




Article

Performance and Mechanism of Fe₃O₄ Loaded Biochar Activating Persulfate to Degrade Acid Orange 7

Qijia Zhu ¹, Kai Zhang ¹, Jiani Xu ¹, Xinyu Wei ¹, Lixia Shi ¹, Sumita ¹, Cong Li ^{1,*} and Eric Lichtfouse ²

¹ School of Environment and Architecture, University of Shanghai for Science and Technology, Shanghai 200093, China; zqj_011126@163.com (Q.Z.); kevin_zhangk@126.com (K.Z.); xujiani07@163.com (J.X.); weixinyuxy@163.com (X.W.); 18985817878@126.com (L.S.); sumita1@163.com (S.)

² State Key Laboratory of Multiphase Flow in Power Engineering, Xi'an Jiaotong University, Xi'an 710049, China; eric.lichtfouse@gmail.com

* Correspondence: congil@aliyun.com

Abstract: Azo dye wastewater is a common type of organic wastewater that often presents a significant challenge due to its gloomy color, high toxicity, and resistance to degradation. The discharge of such wastewater directly into natural water bodies can pose a severe threat to both ecological security and human health. Traditional biological treatment methods are often ineffective in treating industrial pollutants, but advanced oxidation technologies, such as persulfate (PS), offer unique advantages due to their strong oxidation ability and short reaction times. This study investigates the use of modified biochar (BC) material and catalyzed persulfate advanced oxidation technology to adsorb and separate acid orange 7 (AO7), a common industrial pollutant, from water and further oxidize and degrade it. Wood chips were used as biological templates to create an efficient, eco-friendly, and reusable adsorbent and catalytic material. In this paper, the adsorption effect of Fe₃O₄@BC on AO7 in water was compared, the adsorption kinetics and isotherm of Fe₃O₄@BC on different pollutants were studied, and the possible adsorption mechanism was proposed based on the relevant characterization. Adsorption kinetics describes the rate and quality of adsorption by studying the adsorption capacity in the adsorption process. Furthermore, the activated PS system was used to explore the degradation of AO7 at room temperature. First, the catalytic performance of Fe₃O₄@BC was evaluated by examining the amounts of PS and Fe₃O₄@BC, the initial pH, the ionic strength, and the reusability of Fe₃O₄@BC. Then, a possible degradation mechanism was proposed through electron paramagnetic resonance (EPR), free radical quenching experiment, and density functional theory (DFT) analysis. The results of this study suggest that modified biochar material and catalyzed persulfate advanced oxidation technology offer an effective and eco-friendly method for treating AO7 in wastewater.

Keywords: Fe₃O₄ loading; biochar; acid orange 7 (AO7); persulfate (PS); density functional theory (DFT)



Citation: Zhu, Q.; Zhang, K.; Xu, J.; Wei, X.; Shi, L.; Sumita; Li, C.; Lichtfouse, E. Performance and Mechanism of Fe₃O₄ Loaded Biochar Activating Persulfate to Degrade Acid Orange 7. *Water* **2023**, *15*, 1849. <https://doi.org/10.3390/w15101849>

Academic Editor: José Alberto Herrera-Melián

Received: 9 April 2023

Revised: 5 May 2023

Accepted: 10 May 2023

Published: 12 May 2023



Copyright: © 2023 by the authors. Licensee MDPI, Basel, Switzerland. This article is an open access article distributed under the terms and conditions of the Creative Commons Attribution (CC BY) license (<https://creativecommons.org/licenses/by/4.0/>).

1. Introduction

Persulfate-based advanced oxidation process (AOP) is used to degrade pollutants by SO₄^{•−}. It has been fully applied and researched in the aspects of degrading toxic, biodegradable, and persistent emerging organic pollutants, such as pharmaceutical and personal care products (PPCPs), endocrine disrupting chemicals (EDCs), etc. Compared with the advanced oxidative degradation process based on •OH, the advanced oxidative degradation process based on SO₄^{•−} has many advantages. For example, SO₄^{•−} (2.5–3.1V) has a higher redox potential than •OH. In the process of electron transfer, SO₄^{•−} tends to only react with specific organic functional groups. Under certain conditions, SO₄^{•−} has a higher selectivity. Therefore, SO₄^{•−} has a longer half-life than •OH [1,2]. Studies have shown that an advanced oxidation method based on SO₄^{•−} can effectively remove

a variety of refractory organic pollutants in water, such as volatile organic compounds, perfluorinated compounds (PFCs) [3,4], etc.

Persulfate (PS) is a novel type of advanced oxidizer that contains both Peroxymonosulfate (PMS) and Peroxydisulfate (PDS). It is believed to be a derivative of H_2O_2 , with its structure comprising of two sulfonic groups that replace the hydrogens of the two hydroxyl groups in H_2O_2 . Table 1 displays the standard redox potentials of several common oxidants. According to Table 1, the redox potential of PS is second only to F_2 and O_3 . Abiotic wastewater also has an excellent degradation effect. Shah et al. [5] demonstrated that the degradation rate of norfloxacin increased by 19% with the addition of PMS in the solar/BiFe-ZnO system. Kordestani et al. [6] proposed a UV/PDS/ Fe^{2+} system that achieved 97% removal rate of antibiotics within 60 min. The direct oxidation of pollutants in water through PS is relatively slow at room temperature. Therefore, certain methods are frequently used to activate PS to generate $SO_4^{\bullet-}$, which in turn breaks down organic pollutants. Ni et al. [7] found that the PMS/ Co_3O_4 / SnO_2 -8% system had a 92% OFX degradation efficiency within 30 min of catalytic reaction, which was 46 times higher than that of PMS/ SnO_2 alone, and the degradation efficiency could be maintained in a wide pH range (5–11).

Table 1. Common oxidants and their standard electrode potentials.

Oxidants	F_2	O_3	$S_2O_8^{2-}$	HSO_5^-	H_2O_2	MnO_4^-	O_2
Redox potential (V)	2.87	2.07	2.01	1.82	1.78	1.67	1.23

The main metals used to activate PS are transition metal ions with variable valence states, such as Mn^{2+} , Fe^{2+} , Co^{2+} , Cu^+ , Ag^+ , etc. Through the electron transfer process, these metal ions activate PS to form $SO_4^{\bullet-}$. The oxides of these metals also have good PS activation effects. As a heterogeneous catalyst, they do not quench free radicals due to the high concentration of metal ions in the catalytic process. Among metal oxides, iron oxides, such as Fe_3O_4 , Fe_2O_3 , and $FeOOH$, can be used as effective catalysts for the decomposition of H_2O_2 and PS [8,9]. Zhao et al. [10] synthesized nano- Fe_3O_4 -activated PS to degrade p-nitroaniline in wastewater using the co-precipitation method. When the PS dose was 8.0 mM, the Fe_3O_4 dose was 5.32 g/L, the pH was 7, the reaction time was 300 min, the pollutants were completely degraded, and 67% of them were mineralized.

In recent years, carbon materials have been frequently used as catalysts to activate PS for the degradation of organic pollutants. Carbon materials offer several advantages, such as low cost, large surface area, high chemical and thermal stability, and adjustable electrical and physicochemical properties. Activated carbon, carbon nanotubes, graphene, and mesoporous carbon are some examples of carbon materials that have been used for environmental remediation by activating persulfate [11]. Studies have shown that sp² hybrid carbon nanotubes and graphene exhibit higher PS catalytic activity than sp²/sp³ hybridized fullerenes and sp³ hybridized diamond nanocrystals. This suggests that π -electron delocalization systems facilitate the formation of electron-rich edge/vacancy defects at grain boundaries, which promote redox processes [12].

Tang et al. [13] prepared hexagonal ordered mesoporous carbon (CMK-3) and demonstrated that large specific surface area and porous structure can provide more active sites. This increases the contact between active sites and PS molecules, thereby improving the catalytic activity of PS. The study also found that active sites and oxygen-containing functional groups (especially C-OH) perform important roles in the activation of PS by carbon materials. Liu et al. [14] developed a three-dimensional (3D) hollow porous C-doped polymeric carbon nitride (CPCN) catalyst based on the combination of morphological controls and in situ C doping. Among them, in situ C doping can enhance light absorption and promote the charge transfer and separation of the CPCN sample. Duan et al. [15] found a positive correlation between the degree of defects in reduced graphene and the degradation efficiency of phenol. Theoretical calculation results verified that the vacancy and sawtooth/armchair

boundary defects on graphene are important active sites for peroxy bonds in the cracking of PMS. Interaction studies with PMS showed stronger PMS adsorption energy and more efficient electron transfer than graphene-based surfaces. Biochar is a new and popular carbon material that is widely used in catalysis due to its abundant pore structure and a large number of functional groups. It has become a popular material for recent research because the modification range of biological carbon is relatively wide, and the modification conditions can be more selective. To further improve the activation effect of biochar, researchers will adopt various methods to modify it, including morphological regulation, heteroatomic doping, and metal loading. Liu et al. [16] prepared I and P co-doped TiO₂ photoelectrodes, which exhibited preeminent photoelectron catalytic performance for the decomposition of tetracycline hydrochloride. The synergistic effect of I and P co-doping could significantly improve the charge separation rate and enhance the light absorption capacity of TiO₂, leading to an enhancement of PEC activity.

The electron configuration of transition metals typically contains a single electron, which can be readily gained or lost during the activation of PS to form SO₄^{•−}. The purpose of loading metals onto porous materials is to improve catalytic activity, increase utilization efficiency, and reduce metal loss [17]. The most commonly used metal for loading is iron, which includes Fe⁰ [18], Fe₃O₄ [19], γ-Fe₂O₃ [20], FeOOH [21], and FeS₂ [22]. Loading nano ferric oxide onto porous carbon materials promotes a more uniform distribution, enhancing the composite's ability to activate PS.

The activation mechanism of PS by carbon materials can be divided into two categories: the free radical pathway and the non-free radical pathway. The free radical pathway works by breaking the O-O bond in PS to generate SO₄^{•−}, then degrading organic matter. PS can be activated by various components of biochar composites, including functional groups, π-π bonds, defect sites, persistent active substances, and supported metals. Yan et al. [23] found biochar that contains oxygen-containing functional groups, such as hydroxyl and carboxyl groups, can be used as an electron transfer medium to facilitate the decomposition of PS. Huong et al. [24] found that the defective structure of biochar containing carbonyl, carboxyl, and phenol groups enhances the generation of free radicals. In addition, single-bond groups on the surface of carbon materials are oxidized to form active surface groups [25]. The C=C bond is converted into a ketone or quinone group, which can activate PS to produce SO₄^{•−} [26]. Carbon materials with an sp² hybrid structure have many free π electrons. Xu et al. [27] found that pyridine nitrogen with long electron pairs promotes π electron transfer from sp² orbitals of biochar, thus activating PMS and generating SO₄^{•−} and •OH. The defective structure with high electron density distribution in biochar can accelerate electron transfer and provide electrons for PMS activation. Ouyang et al. [28] pointed out that defective structures (edge defects, curvature, or vacancy) produce dangling σ bonds. Thus, their π electrons are not confined to the edge carbon. This makes it easier for biochar to contribute electrons to the PMS to produce SO₄^{•−} and •OH. The persistent active substances in biochar include hemiquinone, phenoxyl, aromatics, etc. These substances can be divided into three categories: free radicals centered on carbon atoms, free radicals centered on oxygen atoms, and free radicals with oxygen functional groups centered on carbon atoms.

Compared with free radical reaction, the non-free radical pathway has several advantages. For example, it can fully utilize the oxidation of PS, eliminate the self-quenching side effects of free radicals, reduce interference from inorganic or organic compounds, operate under a wider range of pH conditions, and potentially select specific pollutants for degradation [29]. The non-free radical pathway involves electron transfer, singlet oxygen, and surface activation. The catalyst acts as an electron conductor, transferring electrons from adsorbed organic pollutants to oxidants through the catalyst surface [30]. This prevents the rapid binding of electrons and hole pairs, thereby increasing catalytic efficiency.

Printing and dyeing wastewater is characterized by complex composition, high organic content, and poor biodegradability. Currently, biological treatment, chemical coagulation, and adsorption methods are used to treat the effluent. However, these methods still leave

behind mature organic matter that is difficult to degrade. Chemical oxygen demand (COD), chroma, and suspended matter levels remain high, making it difficult to meet the enterprise's reuse water quality requirements. Moreover, dye molecules and their degradation products can be carcinogenic, teratogenic, and mutagenic. Acid orange 7 (AO7) is a prime example, which is widely used as an azo dye in the textile, food, and cosmetics industries.

To address these challenges, the current work proposes the use of Fe_3O_4 -biochar composite material for persulfate activation and further formation of $\text{SO}_4^{\bullet-}$ radicals, which will oxidize and thus successfully remove Acid orange 7 dye. In this study, biochar will be doped with iron in order to synthesize Fe_3O_4 -biochar composite materials, which will be used to enhance the highly efficient persulfate activation. This paper also preliminarily evaluates the adsorption capacity of $\text{Fe}_3\text{O}_4@BC$ for AO7 by studying the adsorption kinetics of $\text{Fe}_3\text{O}_4@BC$ for the target pollutants AO7 in order to obtain the adsorption mechanism. The research aims to explore the potential of the rich functional groups on the surface of activated carbon and loaded iron to promote persulfate activation, which will contribute to the oxidation treatment of Acid orange 7. The developed novel technology has significant potential for future practical application.

2. Materials and Methods

2.1. Materials and Methods

Sawdust powder was collected from the local market, repeatedly washed with deionized water and dried naturally in the air. Acid orange 7 (AO7; $\text{C}_{16}\text{H}_{11}\text{N}_2\text{NaO}_4\text{S}$; CAS Number: 633-96-5) was purchased from Shanghai Chemical Reagent Co., Shanghai, China. The initial pH of the solution was adjusted using hydrochloric acid (HCl) or sodium hydroxide (NaOH). All chemicals used in this study were in analytical grade. The deionized water was used for all experiments.

2.2. Preparation Method of $\text{Fe}_3\text{O}_4@BC$

In this paper, the treated sawdust powder was used as raw material. Additionally, it was placed in a tube furnace with continuous nitrogen injection to maintain an oxygen-free condition for pyrolysis. The necessary samples were prepared using the following specific steps. First, the purchased sawdust biochar was soaked in 5% HCl for 24 h to remove impurities, then washed to neutralize ions. Second, the wood chips were placed in a constant temperature blast drying oven at 105 °C for 24 h after completing the cleaning process. Third, the dried sawdust biochar was crushed and treated with a high-speed crusher, then the sawdust powder was prepared for use after a 100-mesh sieve. The wood chip powder obtained was taken in an appropriate amount and placed into a quartz boat, then put into a tubular furnace. After being placed properly, it was passed nitrogen for 30 min to remove most of the air in the pipe. The pyrolysis process is as follows: First, the target temperature was raised to 10 °C/min. It was maintained at a constant temperature for 2 h, then cooled to room temperature naturally. Second, the pyrolyzed biochar was mixed thoroughly with $\text{Fe}(\text{NO}_3)_3 \cdot 9\text{H}_2\text{O}$ in a certain proportion, then pyrolyzed again in the above way to prepare iron-doped $\text{Fe}_3\text{O}_4@BC$ composite material.

2.3. Characterization Methods of Carbon-Based Composites

The surface structure of biochar and its composites were observed using Scanning Electron Microscope (SEM), model Quanta 200 (FEI Company, Hillsboro, OH, USA). Prior to sample testing, the biochar composite was ground and evenly mixed with 10 mL ethanol solution. After the gold spraying treatment, the surface morphology was observed by SEM.

The specific surface area of the biochar was prepared by the Autosorb-1-MP specific surface area analyzer (Quantachrome, Boynton Beach, FL, USA). It was analyzed using the Brunauer–Emmett–Telle (BET) method. The Barrett–Joyner–Halenda (BJH) method was used to calculate the pore size distribution.

The phase structure of the biochar and its composite material was tested by X-ray diffraction (XRD), model D8 ADVANCE (Bruker, Karlsruhe, Germany). The X-ray diffractometer uses Cu anode as a ray source. It has an X-ray wavelength of 0.1542 nm, working current of 45 mA, working voltage of 45 kV, emission slit (ES), anti-scattering slit (SS), and receiving slit (RS) were set at 1° , the scanning speed was $5^\circ/\text{min}$, and the scanning step length was 0.02° . The Scanning range was $10\text{--}90^\circ$.

The Surface functional groups of the prepared catalyst samples were analyzed using Fourier Transform infrared (FTIR) spectroscopy, model Nicolet iS50 (Thermo Fisher Scientific, Waltham, MA, USA). The catalyst samples were processed by potassium bromide (KBr) pressing method with a scanning range of $400\text{--}4000\text{ cm}^{-1}$.

X-ray photoelectron spectroscopy (XPS) was used to analyze the surface element component and valence state of the catalyst. The specific instrument used was the X-ray photoelectron spectroscopy (ESCALAB 250Xi, Thermo Fisher Scientific, Waltham, MA, USA), with an Al $K\alpha$ monochromatic radiation source, and ion source energy $h\nu = 1486.6\text{ eV}$. The test chamber pressure was $9\text{--}10\text{ Torr}$.

2.4. Experimental Steps for Degradation of AO7 by PS

Degradation experiments were carried out in 250 mL conical bottles. The AO7 reaction took place at 298.15 K throughout the entire process. Magnetic agitation, which was applied to the bottom of the conical bottle during the reaction sampling, was conducted at regular intervals. AO7 was sampled, filtered using a $0.45\text{ }\mu\text{m}$ filter, and tested directly on a UV-Vis spectrophotometer. Parallel experiments were conducted 2–3 times for each condition. The reaction solution volume was 200 mL, and pH adjustment was carried out before the reaction using 0.1 mol/L NaOH and H_2SO_4 solutions.

2.5. Free Radical Quencher and Capture Experiment

$\text{SO}_4^{\bullet-}$ and $\bullet\text{OH}$ typically co-exist in the activated PS system of carbon-based materials. To identify the types of free radicals that perform a major role in PS advanced oxidation systems, free radical quenchers were used for quenching experiments. Methanol is a common quencher that can simultaneously quench $\text{SO}_4^{\bullet-}$ and $\bullet\text{OH}$, while tert-butanol is a common $\bullet\text{OH}$ quencher. These quenchers have different rate constants with different free radicals. The reaction rates of methanol with $\text{SO}_4^{\bullet-}$ and $\bullet\text{OH}$ were $3.2 \times 10^6\text{ M}^{-1}\cdot\text{s}^{-1}$, $9.7 \times 10^8\text{ M}^{-1}\cdot\text{s}^{-1}$, respectively. The reaction rates of tert-butanol with $\text{SO}_4^{\bullet-}$ and $\bullet\text{OH}$ are $4\text{--}9.1 \times 10^5\text{ M}^{-1}\cdot\text{s}^{-1}$, $3.8\text{--}7.6 \times 10^8\text{ M}^{-1}\cdot\text{s}^{-1}$, respectively.

The free radical capture experiments were conducted using electron paramagnetic resonance spectroscopy (EPR), model MS 5000 (Bruker, Karlsruhe, Germany). The 5,5-dimethylpyrroline oxide (DMPO) and 2,2,6,6-Tetramethylpiperidine (TEMP) capture agents used in the experiments were refrigerated. In the experiment, the trapping agent and the reaction system were placed in the centrifugal tube with a volume ratio of 1:100 to capture free radicals. Then, the microsolution was injected into the capillary tube and tested in the EPR. The parameters used in the experiment were as follows: The center field intensity was 3510 G, the scanning width was 140 G, the microwave frequency was 9.86 GHz, the microwave intensity was 20.26 mW, the modulation frequency was 100 kHz, and the modulation amplitude was 1.0 G.

2.6. Adsorption Kinetics Theory

Adsorption kinetics is an important aspect of research on adsorption behavior. It describes the rate and quality of adsorption by studying the relationship between adsorption capacity and time in the adsorption process. This section preliminarily evaluates the adsorption capacity of $\text{Fe}_3\text{O}_4@\text{BC}$ on target pollutants AO7 and fully understanding the adsorption process of $\text{Fe}_3\text{O}_4@\text{BC}$ for AO7 in order to obtain the adsorption mechanism.

The adsorption process of the adsorbent and adsorbate can be divided into three stages. The first stage is the external particle diffusion stage, which refers to the process of the adsorbent moving from the solution to the surface of the adsorbent. The second stage is

the intra-particle diffusion stage, which refers to the adsorbate further diffusing from the surface of the adsorbent to the various adsorption points inside the adsorbent. The third stage is the rapid adsorption reaction, which occurs at the effective site. The reaction time at this stage is usually very short, so its influence on adsorption kinetics can be ignored.

2.6.1. Adsorption Kinetics Model

In this experiment, we used a quasi-first-order kinetic model and a pseudo-second-order kinetic model to fit the adsorption kinetic data of AO7. The kinetic adsorption rate constant was determined by using these models.

Pseudo-first-order kinetic model: This model assumes that adsorption is a chemical process, and the main limiting factor is the mass transfer resistance inside the particle. The equation for the pseudo-first-order kinetic model during the adsorption process is as follows:

$$\ln(q_e - q_t) = \ln q_e - k_1 t \quad (1)$$

where, q_e and q_t are, respectively, the adsorption capacity of target pollutants at equilibrium and time t , mg/g; k_1 is the adsorption rate constant in the pseudo-first-order kinetic model, min^{-1} ; and t is the adsorption time, min.

The pseudo-second-order adsorption kinetic model is used when the adsorption process is not only controlled by substance transfer but also by the chemical action of the adsorption process. The equation for the pseudo-second-order kinetic model is as follows:

$$q_t = tk_2q_e^2 / (1 + k_2q_e t) \quad (2)$$

where, q_e and q_t are mg/g of adsorption capacity of target pollutants at equilibrium time and time t , respectively; k_2 rate constant in pseudo-second-order kinetic model, min^{-1} ; and t is the adsorption time, min.

2.6.2. Adsorption Isotherm Model

The adsorption isotherm can study the relationship between the adsorption capacity and the concentration of the adsorbent at a certain temperature, which can reflect the adsorption performance of the adsorbent. By analyzing the experimental data of the adsorption isotherm, relevant parameters of adsorption isotherm can be obtained. These parameters can reflect the structure of the adsorption layer and the adsorption mechanism. Currently, the Langmuir adsorption isotherm and the Freundlich adsorption isotherm are commonly used.

The Langmuir model: Generally, monolayer adsorption on a uniform solid where each adsorption position has the same affinity for adsorbent molecules, and the adsorbed particles are independent of each other.

$$q_e = q_m b C_e / (1 + b C_e) \quad (3)$$

where, q_e represents equilibrium adsorption capacity, mg/g; C_e represents the concentration of the target pollutant at adsorption equilibrium, mg/L; q_m represents the maximum adsorption capacity, mg/g; and b is Langmuir's constant.

Freundlich model: This model assumes that the adsorption process occurs on a heterogeneous phase reaction where the adsorption capacity of the adsorbent surface varies. The concentration of adsorbate on the adsorbent surface increases with an increase in the concentration of the adsorbate.

$$q_e = K C_e^{1/n} \quad (4)$$

where: q_e is the adsorption amount of the target pollutant at adsorption equilibrium, mg/g; C_e is the equilibrium concentration of the target pollutant, mg/L; K is Freundlich's constant; and n is a constant related to adsorption strength.

3. Results

3.1. Determination of Optimal Preparation Conditions for Fe₃O₄@BC

An orthogonal experiment with two factors was designed to determine the optimal conditions for the preparation of Fe₃O₄@BC. These two factors are pyrolysis temperature and the mass ratio of iron/biochar carriers. In order to evaluate the effectiveness of the material's preparation, the adsorption amount of AO7 was chosen as a crucial measure.

The pyrolysis temperature of biochar and the mass ratio of iron/biochar had a significant effect on the adsorption capacity of Fe₃O₄@BC [31]. It can be observed in Figure 1 that the adsorption capacity first increases, then decreases with an increase in the mass ratio of iron/biochar. The addition of iron facilitates the decomposition of biochar. Moreover, loading iron enhances the adsorption performance. However, excess iron can lead to the blocking of the biochar pores. The effect of pyrolysis temperature on the adsorption capacity showed a similar trend. Increasing the pyrolysis temperature may promote the decomposition of organic compounds in biochar, which increases its surface area and pore structure. This benefits the increase in adsorption sites. However, with further rising of the temperature, the structure of biochar may be completely destroyed, which affects the adsorption effect [32]. Thus, the maximum adsorption capacity of AO7 at 13.85 mg/g was obtained under the optimal preparation conditions of iron/biochar mass ratio at 0.8 and pyrolysis temperature at 650 °C.

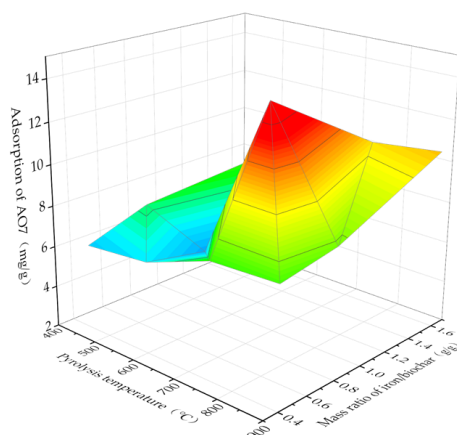


Figure 1. Influence of pyrolysis temperature and iron/biochar mass ratio of magnetic biochar material on the adsorption of AO7.

3.2. Characterization of Fe₃O₄@BC

3.2.1. XRD Analysis

The iron loading on the biochar was determined by XRD patterns. The crystal structures of biochar and Fe₃O₄@BC before and after activation of PS were analyzed. As shown in Figure 2, there is a diffraction peak at $2\theta = 26.2^\circ$, which is related to the (002) characteristic plane of the graphite structure. It shows that after pyrolysis and carbonization of biomass, a certain order of graphite structure is formed. Six distinct diffraction peaks appeared at 30.1° , 35.7° , 43.5° , 53.4° , 57.6° , and 62.9° , which can be attributed to (220), (311), (400), (422), (511), and (440) of Fe₃O₄ spinel structures, respectively [33]. In contrast, the characteristic peaks of Fe and its oxides did not appear clearly in the XRD pattern phase of the undoped biochar. This demonstrates that Fe(NO₃)₃·9H₂O was mainly converted to Fe₃O₄, which was loaded onto the biochar during the pyrolysis process. The sharp peak shape indicates that the crystal form of Fe₃O₄ is complete, which means the particle size of Fe₃O₄ loaded on the surface of biochar is uniform. Additionally, since the peak position of Fe₃O₄ did not change significantly before and after the activation of PS by Fe₃O₄@BC, it indicates that the material has a stable crystal structure [34]. The slight change in peak abundance indicates that Fe₃O₄ performs a role in this catalytic reaction.

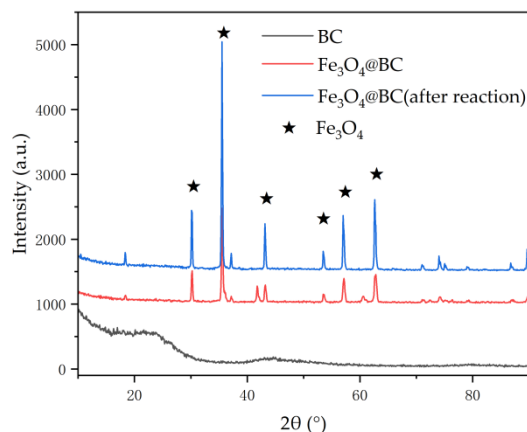


Figure 2. XRD patterns of undoped iron biochar and $\text{Fe}_3\text{O}_4@BC$ samples.

3.2.2. Surface Element Valence Analysis

A survey using XPS was conducted to investigate the composition and chemical states of the prepared biochar samples. As shown in Figure 3, two main peaks were observed at 710.52 and 724.12 eV, corresponding to Fe $2p_{3/2}$ and Fe $2p_{1/2}$, respectively [35]. It was confirmed that the iron ions were in the trivalent form of oxidation. By comparing the XPS images of the biochar before and after activation of PS, it can be concluded that the peak intensities at Fe $2p_{3/2}$ and Fe $2p_{1/2}$ of $\text{Fe}_3\text{O}_4@BC$ decreased after activation. On the one hand, this indicates that after activation of PS, some loaded iron and its oxides permeate into the reaction solution, but most of it remains on the biochar. On the other hand, the low-valent iron ions in $\text{Fe}_3\text{O}_4@BC$ can transfer electrons to PS to generate Fe^{3+} , and Fe^{3+} can also activate PS to generate $\text{S}_2\text{O}_8^{\bullet-}$ and Fe^{2+} [36].

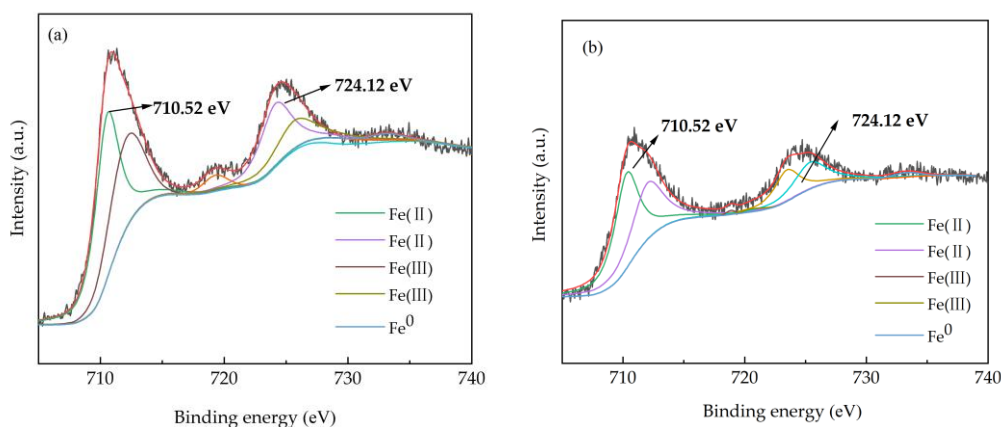


Figure 3. XPS spectra of magnetic biochar before reaction (a) and magnetic biochar samples after reaction (b).

3.2.3. Surface Chemical Functional Group Analysis

The changes in functional groups of the undoped iron biochar and $\text{Fe}_3\text{O}_4@BC$ were analyzed by using the FTIR technique. The FTIR characterization is presented in Figure 4. The FTIR spectra of $\text{Fe}_3\text{O}_4@BC$ showed a significantly enhanced intensity at 1580 cm^{-1} (C=O) and 3424 cm^{-1} (O-H) compared to the undoped iron biochar. This indicates an increase in the corresponding functional groups on the material surface. The absorption peak at 1622 cm^{-1} is the vibration peak of the sp_2 hybrid carbon-nitrogen double bond -C=N . A broad absorption peak appears at 1047 cm^{-1} , which is the absorption peak caused by Si-O-Si asymmetric stretching vibration and Si-O-C. The biochar prepared by pyrolysis after loading Fe showed an obvious absorption peak at 636 cm^{-1} , which was caused by the stretching vibration of octahedral Fe^{3+} (Fe-O mode). This indicates that the material

successfully loaded Fe and formed Fe-containing functional groups. Meanwhile, $\text{Fe}_3\text{O}_4@\text{BC}$ showed an absorption peak of the Fe-O bond at 580 cm^{-1} , which is the characteristic absorption band of Fe_3O_4 [37]. This demonstrates the formation of Fe_3O_4 during the pyrolysis after the application of $\text{Fe}(\text{NO}_3)_3\cdot 9\text{H}_2\text{O}$ [38].

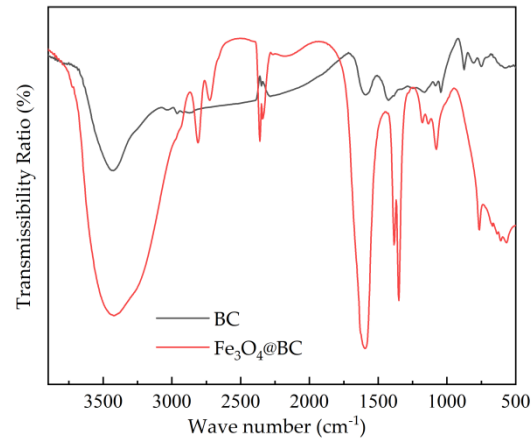


Figure 4. FTIR spectra of undoped iron biochar and magnetic biochar samples.

3.2.4. Microscopic Morphological Characteristics

The surface morphological characteristics of the undoped iron biochar and $\text{Fe}_3\text{O}_4@\text{BC}$ are shown in Figure 5. As shown in Figure 5a, the undoped Fe biochar presented a flat and smooth surface with an inconspicuous pore structure. After mixing $\text{Fe}(\text{NO}_3)_3\cdot 9\text{H}_2\text{O}$ solid for secondary pyrolysis, the surface morphological characteristics of $\text{Fe}_3\text{O}_4@\text{BC}$ are shown in Figure 5a. Such a structure exposed more available adsorption sites, which facilitated the subsequent adsorption degradation of the contaminants. The changes in the surface morphology of $\text{Fe}_3\text{O}_4@\text{BC}$ before and after the activation of persulfate are compared in Figure 5b,c. It can be seen that there is a significant reduction in the surface cluster structure after oxidation. This indicates that the magnetic biochar participated in the catalytic process [39].

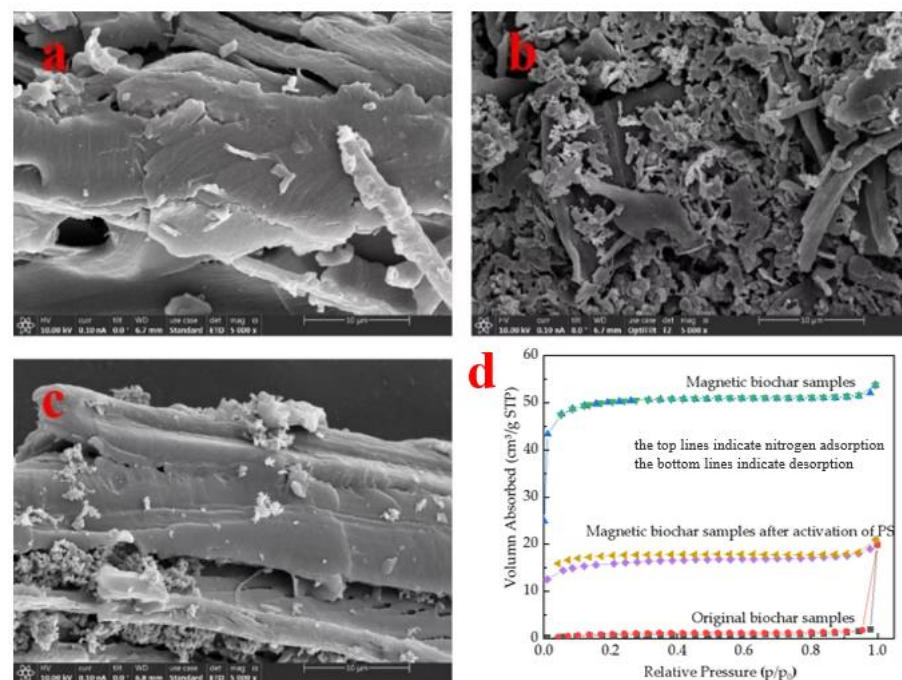


Figure 5. SEM images of original biochar samples (a), magnetic biochar samples (b), magnetic biochar samples after activation of PS (c), and BET nitrogen adsorption isotherm (d).

Figure 5d investigates the specific surface area and pore characteristics of undoped iron biochar and Fe₃O₄@BC by using nitrogen adsorption/desorption isotherms. From the isotherm curves, it can be observed that the curves have the type IV characteristic of the H4 hysteresis loop. This demonstrates the presence of micropores and mesopores on the surfaces of undoped iron biochar and Fe₃O₄@BC. The specific surface areas of Fe₃O₄@BC before and after the activated persulfate reaction were 158.99 m²/g and 46.70 m²/g, respectively. The large specific surface area of Fe₃O₄@BC before the activation reaction may be due to the successful attachment of Fe₃O₄ particles on BC [40]. Meanwhile, since the catalytic reaction is a surface-controlled process, the increase in catalyst surface area generates more active sites on the surface [41]. The specific surface area became smaller after the activated persulfate reaction, probably due to the adsorption of some AO7 on the surface. The total pore volumes before and after the reaction were 0.083 cm³/g and 0.032 cm³/g, respectively.

3.3. Adsorption Performance of Fe₃O₄@BC

3.3.1. Analysis of Adsorption Kinetics Fitting Results

The results of the pseudo-first-order kinetic model and pseudo-second-order kinetic model fit for the adsorption of AO7 by Fe₃O₄@BC are displayed in Figure 6. The correlation coefficient R² of the pseudo-second-order kinetic model for the Fe₃O₄@BC adsorption on AO7 is 0.98, which is close to the pseudo-first-order kinetic parameters (0.97) presented in (Table 1). Additionally, the two adsorption kinetic models fit well. Thus, the pseudo-first-order and pseudo-second-order kinetic models both fit to describe the adsorption process of AO7 by Fe₃O₄@BC [42]. The equilibrium adsorption capacity of AO7 was found to be 9.37 mg/g and 11.83 mg/g after 90 min of adsorption through the calculation of two different models.

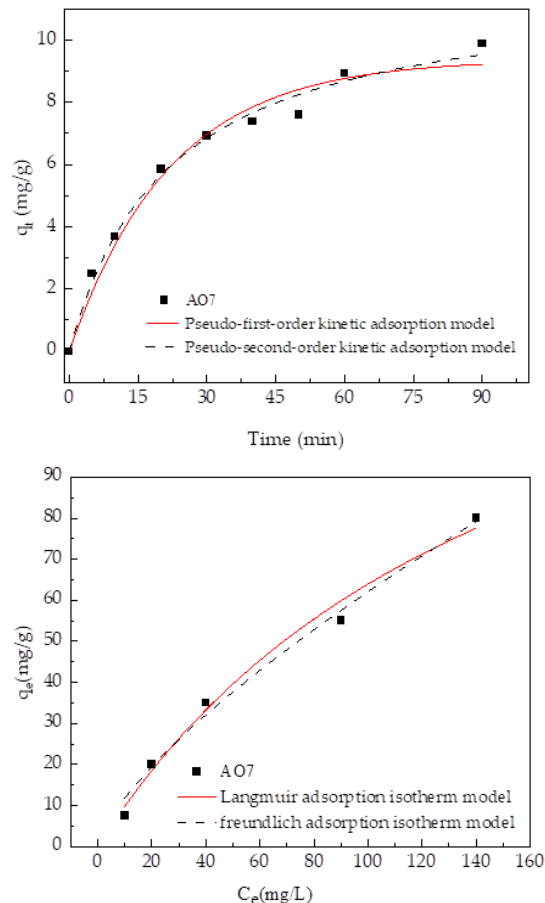


Figure 6. The fitting curves of adsorption kinetics and adsorption isotherms for AO7.

The pseudo-second-order kinetic adsorption model is based on the assumption of chemisorption, suggesting that chemisorption occurs during the adsorption process of AO7 by Fe₃O₄@BC. In this study, AO7 was presented as an anion under the adsorption conditions, while Fe₃O₄@BC had a positive surface charge under the same conditions. Therefore, the adsorption effect of AO7 was enhanced through electrostatic interaction [36]. The pseudo-first-order kinetic fitting results indicate that physical adsorption also existed during the process of Fe₃O₄@BC adsorption of AO7. The adsorption is greatly affected by the concentration of the substance and the effect of mass transfer.

3.3.2. Analysis of Fitting Results of Adsorption Isotherm

The relationship between the amount of AO7 adsorbed by Fe₃O₄@BC and the equilibrium concentration is shown in Figure 7. Within the studied concentration range, the adsorption capacity of Fe₃O₄@BC on AO7 increased from 7.5 mg/g to 85 mg/g.

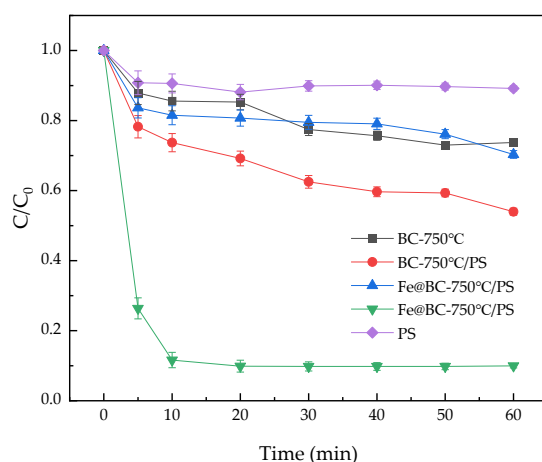


Figure 7. Effect of different systems on the removal of AO7.

To further investigate the adsorption behavior of Fe₃O₄@BC on AO7, both Langmuir and Freundlich isotherm models were used to fit the adsorption data. As shown in Table 2, the fitted parameters R² of both Langmuir and Freundlich adsorption isotherm models for AO7 were greater than 0.96, indicating the existence of both monolayer and multilayer adsorption behaviors of Fe₃O₄@BC in the adsorption of AO7 [43,44].

Table 2. Kinetic model and isotherms model fitting parameters for the adsorption of AO7 by biochar samples.

	Model	Parameter	AO7
kinetic model	pseudo-first-order kinetic adsorption model	k_1 (min ⁻¹)	0.045
		q_e (mg/g)	9.37
		R^2	0.97
	pseudo-second-order kinetic adsorption model	k_2 (min ⁻¹)	0.0038
		q_e (mg/g)	11.83
		R^2	0.98
isotherms model	Langmuir adsorption isotherm model	K_L (min ⁻¹)	0.006
		n	165.8
		R^2	0.98
	Freundlich adsorption isotherm model	K_F (min ⁻¹)	2.23
		n	1.38
		R^2	0.98

This section utilizes Fe₃O₄@BC activated PS to degrade simulated wastewater containing AO7, based on the unsatisfactory adsorption effect of Fe₃O₄@BC on AO7. The factors

that affect the oxidation efficacy include the initial concentration of AO7, Fe₃O₄@BC dosage, PS dosage, initial pH, and inorganic anions. Additionally, the reusability of Fe₃O₄@BC, the variation of Fe²⁺ in the system, the variation of TOC, and the possible bond-breaking sites of AO7 molecules were inferred based on the DFT analysis results of AO7.

3.4. Removal Effect for AO7 of the PS System Catalyzed by Fe₃O₄@BC

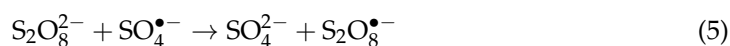
The experiments were conducted on five different systems: biochar, BC/PS, Fe₃O₄@BC, Fe₃O₄@BC/PS, and PS. The objective was to observe the influence of these different systems on the removal effect of AO7. The operating conditions were as follows: the dosage of PS was 15 mM; the dosage of Fe₃O₄@BC was 2 g/L; and the initial concentration of AO7 dye was 50 mg/L. The results of the experiments are shown in Figure 7. The result of control experiments showed that the system of Fe₃O₄@BC coupled with PS significantly enhanced the removal effect of AO7. In the first 10 min of the reaction, the removal rate of AO7 was approximately 85%. After 20 min, when the reaction was almost completed, the removal efficiency was about 90%.

In the BC/PS system, it was evident that the degradation effect of the system on AO7 exceeded that of the other three kinds of systems, which were single BC, Fe₃O₄@BC, and PS, respectively. This finding confirmed that biochar, even without doping, performed a role in activating PS. However, its activation was not good as Fe₃O₄@BC. This was because the Fe₃O₄@BC composite materials, which utilized the synergistic effect of carbon and iron, destroyed O-O bond in PS to generate SO₄^{•-} in the process of activating PS [45]. Related studies have shown that RuO₂-AC/PMS system can remove phenol better than RuO₂ zeolite/PMS system. This is because the adsorption ability of AC promotes the surface reaction of the reactive groups with phenol [46].

The operating conditions during the reaction process had a greater influence on the reaction results. The part investigated some elements to further explore the degradation efficiency of the Fe₃O₄@BC/PS system on AO7, including dosage of PS and Fe₃O₄@BC, initial pH, initial concentration of AO7, and so on.

3.4.1. Effect of PS Dosage

The PS dosage had a significant influence on the capacity to oxidize and degrade AO7, and the operating costs of the system. For the degradation experiments, the initial concentration of PS was set to 3, 9, 15, 21, and 27 mM, while the concentration of Fe₃O₄@BC was held constant at 0.5 g/L. The purpose was to investigate the effect of PS concentration on AO7 degradation efficiency, and the results are shown in Figure 8a. The removal efficiency of AO7 showed a significant improvement with increasing PS dose. When the PS dosage was 15 mM, the degradation efficiency of the system on AO7 achieved its best level with a degradation efficiency of 90% in 1h of reaction time. However, the removal efficiency of AO7 showed a decreasing trend as the PS dosage increased continuously. This may be due to the quenching reaction of PS itself, which causes the concentration of SO₄^{•-} to decrease with increasing PS concentration [47]. Therefore, the removal efficiency becomes lower (Equations (5) and (6)).



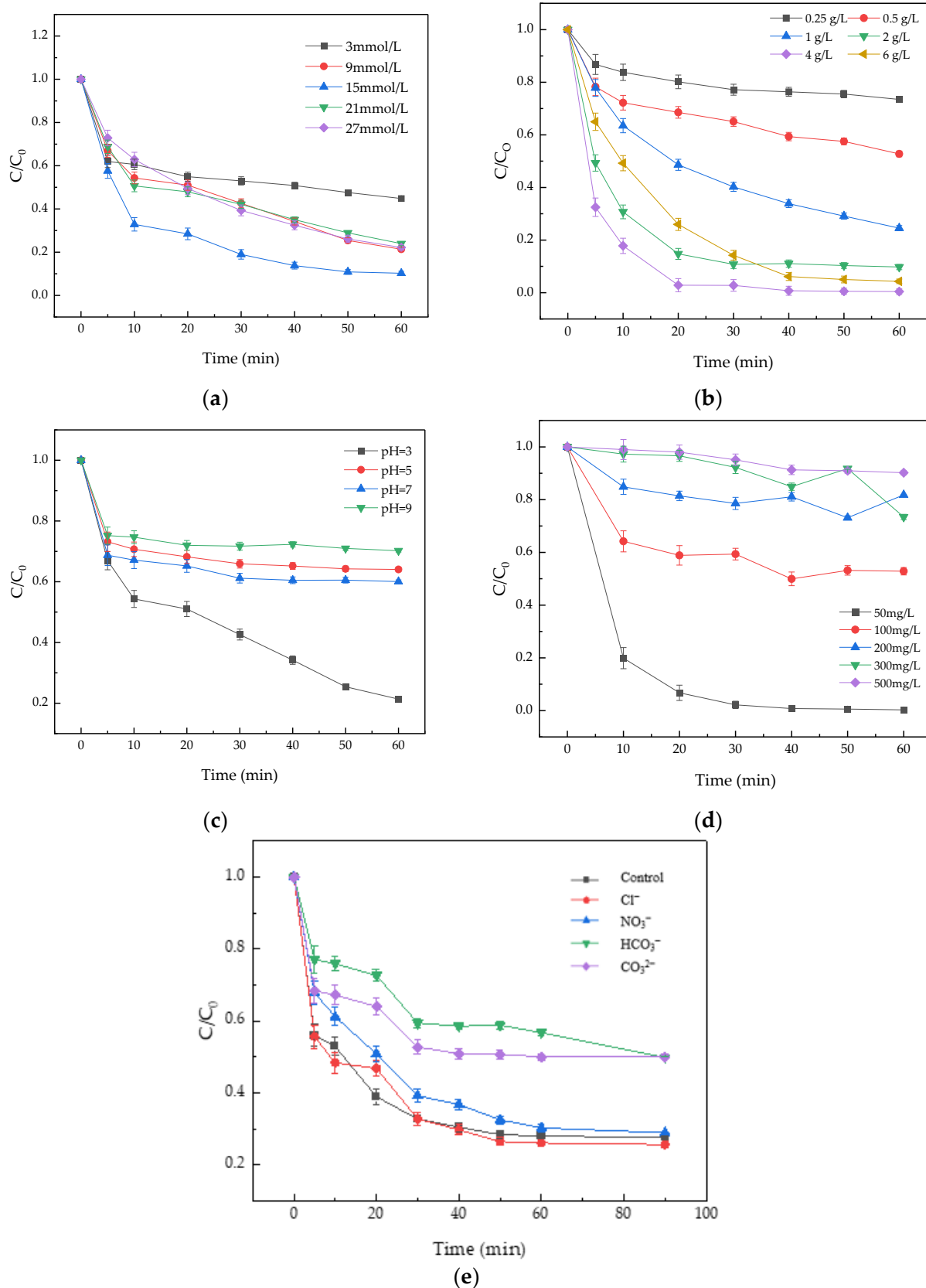


Figure 8. Effects of different reaction conditions on AO7 degradation in the Fe₃O₄@BC/PS. (a) PS dosage (from 3 to 27 mM); (b) Fe₃O₄@BC dosage (from 0.25 to 6 g/L); (c) Initial pH (from 3 to 9); (d) Initial concentration of AO7 (from 50 to 500 mg/L); and (e) Different inorganic anions.

3.4.2. Effect of Fe₃O₄@BC Dosage

To investigate the influence of Fe₃O₄@BC dosage on the degradation effect of AO7, degradation experiments were carried out at different dosages of Fe₃O₄@BC, specifically 0.25, 0.5, 1, 2, 4, and 6 g/L. The experimental conditions included an initial concentration of AO7 at 50 mg/L and a PS dosage of 3 mM.

The results showed that the removal efficiency increased gradually with increasing Fe₃O₄@BC dose from 0.25 g/L to 4 g/L, as shown in Figure 8b. On the one hand, increasing the Fe₃O₄@BC dosage led to greater pollutant removal due to the adsorption effect. On the other hand, increasing the catalyst dosage provided more active sites resulting in better PS activation. Moreover, it has been shown that the more Fe₃O₄ loaded on the catalyst surface, the more active sites are created. This can be effectively used by PMS to promote more SO₄^{•−} production [48]. Notably, the increase in removal efficiency was relatively large with increasing Fe₃O₄@BC dose during the process. However, the initial efficiency of AO7 degradation reaction decreased when the catalyst dosage was 6 g/L. This was due to the leached Fe²⁺ reacting directly with SO₄^{•−} formed in the system, preventing it from reacting with the target pollutant. Additionally, excess SO₄^{•−} formed on the surface of the catalyst, creating an excessively oxidized environment. This reduced the capacity of Fe₃O₄@BC to activate SO₄^{•−}, as the surface had already been oxidized.

3.4.3. Effect of Initial pH

The Fe₃O₄@BC/PS system produced different kinds of free radicals under different pH conditions, which affected its oxidation properties. Therefore, the initial pH was a critical factor in the degradation system. In the AO7 degradation experiments, the initial pH in the solution was set to 3, 5, 7, and 9, respectively, to investigate the influence of the AO7 degradation efficiency under different initial pH conditions. The pH of the system was regulated using 1 M HCl and 1 M NaOH in the research. Figure 8c shows the AO7 removal by the Fe₃O₄@BC/PS system under different initial pH conditions. It can be observed that the system's removal efficiency on AO7 was approximately 90% after 1 h of reaction at pH 3. The surface of biochar was positively charged when the pH of the solution was less than the pHPZC, and it was negatively charged when the pH was greater than the pHPZC [49]. In the experiment, the pHPZC of Fe₃O₄@BC was 4.88. Therefore, Fe₃O₄@BC was positively charged when the pH was less than 4.88 and negatively charged when the pH was more than 4.88. Meanwhile, AO7 could be adsorbed on the surface of Fe₃O₄@BC when the pH was less than 4.88 because it was an anionic dye, and there was an electrostatic attraction between the catalyst and pollutant.

3.4.4. Effect of AO7 Initial Concentration

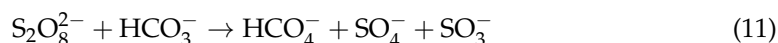
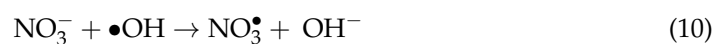
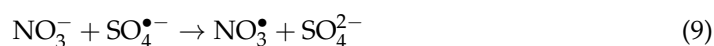
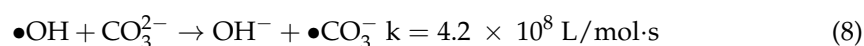
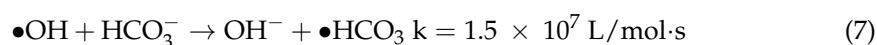
The concentration of the reaction substrate was a significant factor that affected the degradation effect. As shown in Figure 8d, different initial concentrations of AO7 had an influence on AO7 degradation by the Fe₃O₄@BC/PS system. The efficiency of AO7 removal decreased with an increase in AO7 concentration from 50 mg/L to 500 mg/L. When the initial concentration of AO7 was 50 mg/L, the AO7 removal efficiency was about 98% in 60 min. However, the degradation effect of the system on AO7 was almost negligible when the concentration of AO7 increased to 300 mg/L or above. This was due to the concentration of free radicals being limited under degradation conditions, which was not enough to degrade dyes with high concentrations [50]. The degradation efficiency decreased in the initial reaction stage when the AO7 concentration increased from 50 mg/L to 100 mg/L. The removal efficiency of AO7 was about 50% after reacting for 1 h. Extending the reaction time further improved the removal efficiency of the AO7 solution with 100 mg/L.

3.4.5. Effect of Inorganic Anions on AO7 Removal

The natural water contained a significant amount of inorganic anions, such as Cl[−], NO₃[−], CO₃^{2−}, HCO₃[−], and others. These anions could potentially compete with organic

pollutants in the water for free radicals, leading to a decrease in pollutant removal efficiency [51]. However, these anions could also react with other substances and produce other kinds of free radicals, which could accelerate the degradation process. Therefore, it was essential to investigate the effect of inorganic anions on the oxidation degradation system. For example, both HCO_3^- and CO_3^{2-} could react with $\text{SO}_4^{\bullet-}$ to generate other free radicals with lower oxidation potentials [52]. In the experiments, several common inorganic anions, including Cl^- , CO_3^{2-} , NO_3^- , HPO_4^{2-} , and others, were selected to explore their effect on the PS system's oxidability activated by $\text{Fe}_3\text{O}_4@\text{BC}$. The results are presented in Figure 8e.

The figure showed that the presence of CO_3^{2-} and HCO_3^- inhibited AO7 degradation by the system, as these anions reacted with free radicals in the system. Specifically, $\bullet\text{OH}$ reacted with CO_3^{2-} and HCO_3^- to form other radicals, as shown in Equations (7) and (8). The AO7 removal efficiency decreased due to the competition for free radicals by inorganic anions. A similar inhibitory effect was observed in the presence of NO_3^- , although it was not as evident as the effect of CO_3^{2-} and HCO_3^- . NO_3^- reacted with $\bullet\text{OH}$ and $\text{SO}_4^{\bullet-}$ to generate NO_3^\bullet with lower oxidation activity, respectively. On the other hand, Cl^- acted as an activated solvent, improving the degradation efficiency of the $\text{Fe}_3\text{O}_4@\text{BC}/\text{PS}$ system on the substrate.



3.5. Changes of TOC in the AO7 Degradation Process

The AO7 removal and mineralization efficiency in the process of $\text{Fe}_3\text{O}_4@\text{BC}/\text{PS}$ system degrading AO7 is shown in Figure 9. The AO7 removal efficiency was mainly measured by the decolorization degree of the AO7 solution, while the mineralization efficiency was measured by the degree of TOC removal. Initially, there was a fast AO7 removal efficiency which declined exponentially over time, while the TOC removal efficiency was slowed in the initial stage. After 20 min of reaction, the AO7 removal efficiency was about 90%, while the TOC removal efficiency was approximately 17%. However, the TOC removal efficiency increased gradually from 17% to the final 30%. The mineralization effect primarily depended on free radicals, with $\text{SO}_4^{\bullet-}$ reacting with intermediate products (cyclodiene) to generate derivatives of dicarboxylic acids (such as acetic acid), while H_2CO_3 and CO_2 were eventually formed. In the process of AO7 oxidation degradation by the $\text{Fe}_3\text{O}_4@\text{BC}/\text{PS}$ system, the main effect was the destruction of the -N=N- bond of the azo dye to achieve the purpose of removing chromaticity. However, it should be noted that huge amounts of intermediate products were not mineralized in the system.

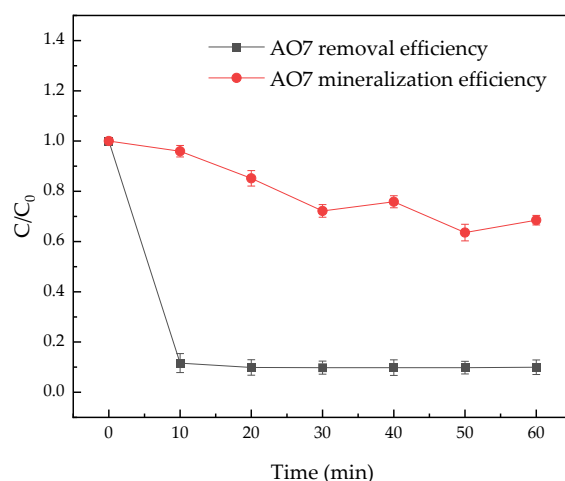


Figure 9. Changes of TOC during the degradation of AO7.

3.6. Degradation Mechanism of AO7 by Fe₃O₄@BC/PS System

The modified biochar material catalyzes persulfate to generate strong oxidizing free radicals, such as SO₄^{•−} and •OH. This provides an effective and eco-friendly method for treating AO7 in wastewater. In order to further explore the degradation of the process, a possible degradation mechanism was proposed through electron paramagnetic resonance (EPR), free radical quenching experiment, and density functional theory (DFT) analysis. The mechanism diagram of the enhanced degradation performance caused by Fe₃O₄ loading is shown in Figure 10.

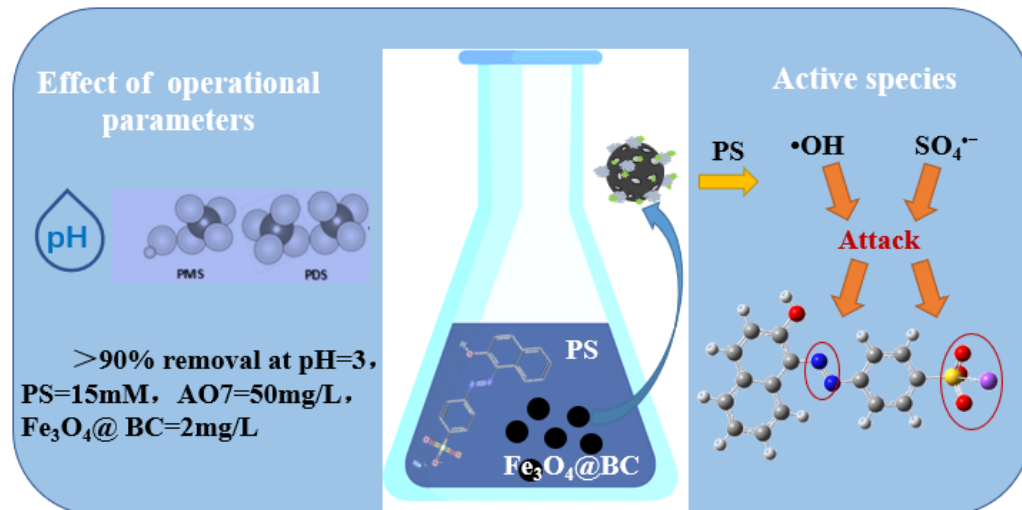


Figure 10. Mechanism diagram of the enhanced degradation performance caused by Fe₃O₄ loading.

3.6.1. Free Radical Quenching Experiment

According to records, alcohol-containing α -H, such as carbinol and MeOH, have high reactivity with •OH and SO₄^{•−} free radicals. They can quickly capture these two radicals to form inactive intermediates, thereby ending the reaction between free radicals and substrate. Tert-butanol(TBA) is an excellent free radical trapping agent [53]. The reaction rate constant of TBA with •OH and SO₄^{•−} are $5 \times 10^8 \text{ M}^{-1} \cdot \text{S}^{-1}$ and $4 \times 10^5 \text{ M}^{-1} \cdot \text{S}^{-1}$, respectively [54,55]. Clearly, the reaction rate constant with SO₄^{•−} is three orders of magnitude lower than •OH. Therefore, MeOH and TBA can be used as quenching agents for free radicals. The two quenching agents reacted with •OH and SO₄^{•−} at different rates. Hence, we can use it to verify which radicals perform a major role in the system.

In the free radicals experiment, three groups of the experiment were set up: blank control group, methanol quenching agent group, and TBA quenching group. The experimental conditions of the blank control group adopted the best experimental parameters determined above. The ratio of the quenching agent and PS is 20:1. The experimental results are shown in Figure 11. Compared with the blank control group, both kinds of quenching agents inhibited the degradation of AO7 to a certain extent, indicating that $\bullet\text{OH}$ and $\text{SO}_4^{\bullet-}$ simultaneously perform a degradation role in this system [26,56]. The quenching effect of TBA and MeOH with the same molar ratio was compared, and it was found that the inhibition effect of the TBA system was greater than the MeOH system. This proves that $\bullet\text{OH}$ performs a major role in the degradation of AO7 in this system, while $\text{SO}_4^{\bullet-}$ performs an auxiliary role.

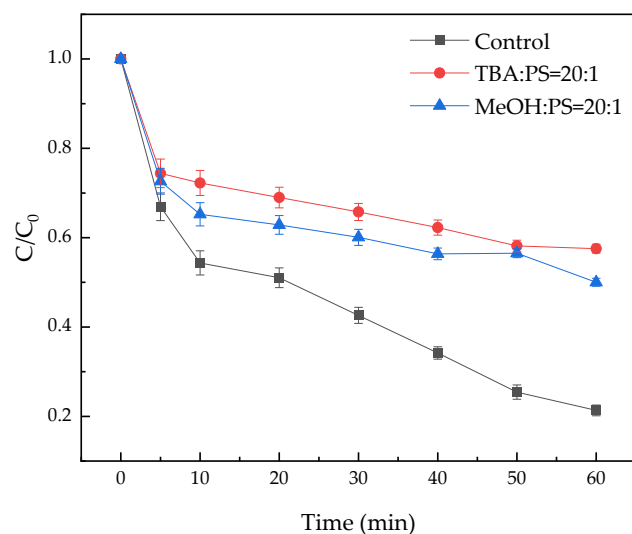


Figure 11. Effect of different free radical quenchers on the quenching of the reaction system.

3.6.2. Identification of Free Radicals in the System by EPR Technology

EPR is currently considered one of the most effective methods for detecting free radicals. In the degradation experiment of AO7 by $\text{Fe}_3\text{O}_4@\text{BC}/\text{PS}$ system, DMPO, and TEMP free radical trapping agents were used to capture free radicals under $\text{pH} = 3$ conditions. The experimental results, shown in Figure 12, indicate that when using the DMPO capture agent, distinct spectral characteristic signal peaks of DMPO- $\bullet\text{OH}$ and DMPO- $\text{SO}_4^{\bullet-}$ adducts can be observed, with signal intensity ratios of approximately 1:2:2:1 and 1:1:1:1:1:1, respectively [57–60]. Under the same experimental conditions, using TEMP free radical trapping agent to capture $^1\text{O}_2$, the obvious TEMP- $^1\text{O}_2$ signal can be seen, and its intensity ratio is 1:1:1.

3.6.3. AO7 Density Functional Calculation

The Electronic Structure of the AO7 Molecule was calculated using the DFT method to explore its chemical reactivity and explain its reaction mechanism. The atomic-level prediction of the reaction sites was carried out as described in references [57–60]. Figure 13a shows the optimal molecular configuration of the AO7 molecule, while Figure 13b shows the charge distribution of each atom within the molecule. The charge distribution diagram provides an indication of the reaction activity of different parts of the molecule. The atom with the lowest negative charge is O33 (−0.646), while the atom with the highest positive charge is S31 (1.216). Moreover, the large potential difference between the C26-S31 bond renders it highly susceptible to cleavage, resulting in the formation of new intermediates.

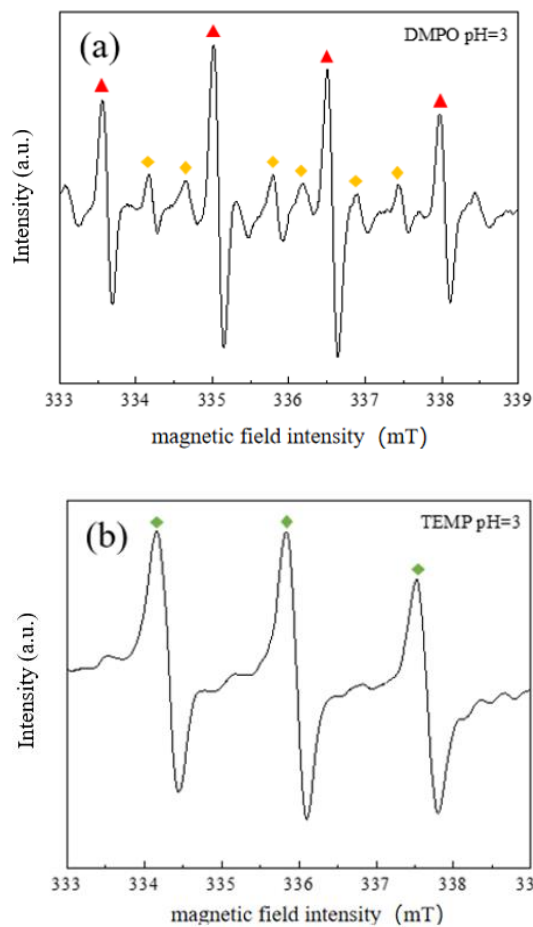


Figure 12. Electron paramagnetic resonance spectra of DMPO (a) and TEMP (b) trapping agent in magnetic biochar/PS degraded AO7 system.

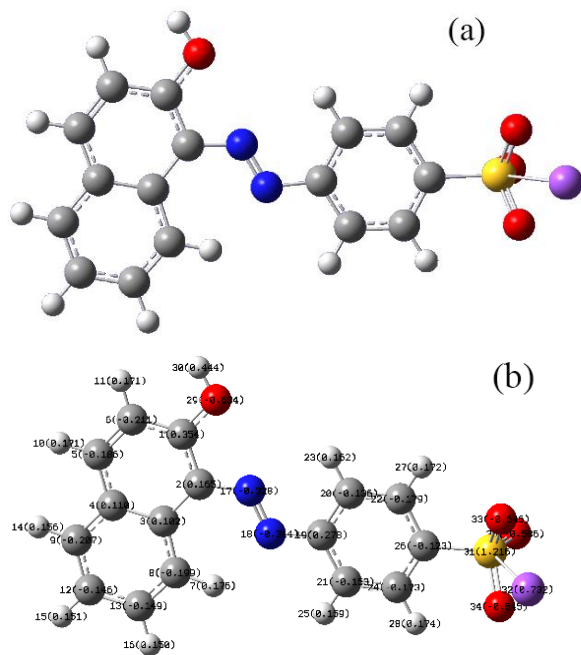


Figure 13. Optimal molecular conformation (a) and AO7 molecular charge distribution (b).

However, the charge distribution map can only preliminarily reflect the information regarding the chemical bonds that may be easily broken within the molecule. It cannot accurately reflect the possible attack sites of active species at the molecular level. The electrostatic potential diagram of the molecule is more helpful in predicting the reaction site. Figure 14 shows the electrostatic potential (ESP) diagram of the AO7 molecule. On the ESP map, the most electronegative regions are most susceptible to attack by electrophiles. For AO7, the minima on the ESP plot are near N17-N18, O33, O34, and O35, indicating that these atoms are more susceptible to attack by electrophiles ($\text{SO}_4^{\bullet-}$, $\bullet\text{OH}$, and O_2^-). The results of EPS can be further analyzed and interpreted using the Fukui function. According to the frontier molecular orbital theory, the highest occupied molecular orbital (HOMO) and the lowest unoccupied molecular orbital (LUMO) can provide more information to predict the reactive sites [61,62]. Figure 15 shows the HOMO and LUMO orbitals of AO7. The HOMO electron cloud is mainly distributed at C1, C2, C9, C12, C5, C8, and N18, indicating that these sites are prone to oxidation reactions. The electron cloud of LUMO is mainly distributed in C1, C5, N17, and C19, indicating that these sites are prone to reduction reactions.

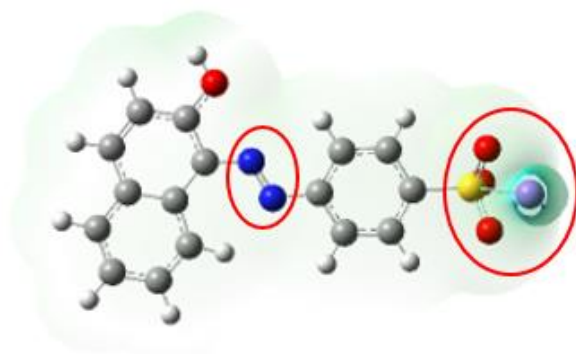


Figure 14. Electrostatic potential diagram of AO7 molecule.

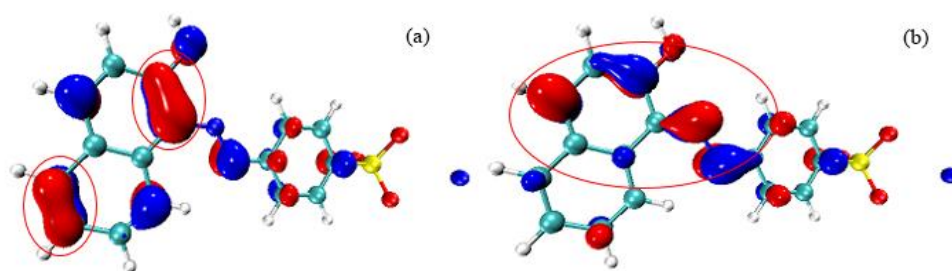


Figure 15. HOMO (a) and LUMO (b) orbitals of AO7 molecule.

3.7. Leaching of Fe^{2+} and Stability of Catalyst from the System of $\text{Fe}_3\text{O}_4@\text{BC}/\text{PS}$ Degradation of AO7

Figure 15 shows the changes in Fe^{2+} ion concentration during the degradation of AO7 by the $\text{Fe}_3\text{O}_4@\text{BC}/\text{PS}$ system. During the first stage, the $\text{Fe}_3\text{O}_4@\text{BC}$ composite gradually released Fe^{2+} into the system as a heterogeneous catalyst within 0–20 min. Consequently, the concentration of Fe^{2+} gradually increased, which became the primary iron ion in the system. The Fe^{2+} released into the system acts as an electron donor, providing electrons to AO7 molecules and activating PS. As a result, Fe^{2+} is gradually converted into Fe^{3+} , and the concentration of Fe^{2+} is gradually reduced. This finding aligns with the earlier experimental conclusion that Fe (II) and oxidized functional groups are activated throughout the process [26]. The concentration of Fe^{2+} reaches its maximum at 20 min in Figure 16, which is consistent with the previous article's experimental observation that AO7 reaches optimal degradation rates around 20 min.

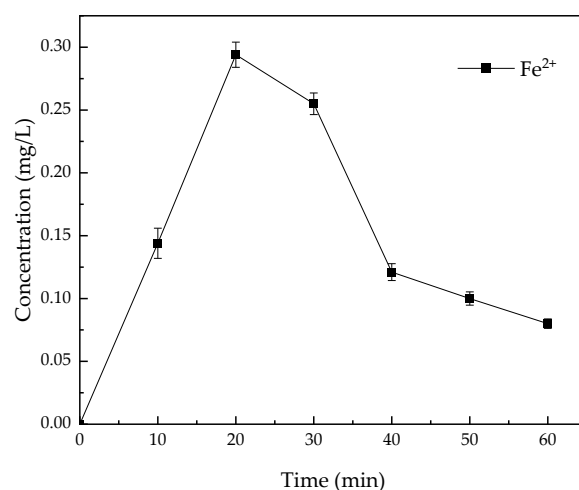


Figure 16. Concentration changes of Fe^{2+} .

The reusability of catalysts is a crucial factor in evaluating their potential for practical applications. Figure 17 shows the removal rate of AO7 by PS, which was reactivated using $\text{Fe}_3\text{O}_4\text{@BC}$. The removal efficiency of AO7 decreased significantly after each reuse cycle [63,64]. Initially, when the catalyst was first used to activate PS for degrading AO7, the removal rate could reach approximately 80%. However, after the first reuse, the removal rate dropped to around 40%. The effective iron-based components of $\text{Fe}_3\text{O}_4\text{@BC}$ were oxidized to ferric iron during the cyclic activation of PS, while the oxygen-containing functional groups on the surface of biochar were consumed. Consequently, in the second reuse, the removal rate of AO7 was only about 10%.

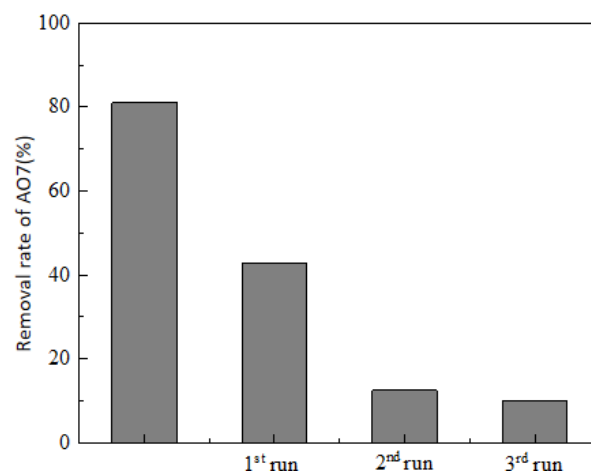


Figure 17. Reuse of magnetic biochar.

4. Conclusions

The optimum pyrolysis temperature for preparing $\text{Fe}_3\text{O}_4\text{@BC}$ is $650\text{ }^\circ\text{C}$, with a mass ratio of iron to carbon is 0.8. At this temperature, the adsorption amount of AO7 is the highest at 13.85 mg/g , and the specific surface area of $\text{Fe}_3\text{O}_4\text{@BC}$ reaches $158.99\text{ m}^2/\text{g}$. XRD and SEM patterns confirmed the successful loading of Fe_3O_4 on the biochar template; $\text{Fe}_3\text{O}_4\text{@BC}$ had a large specific surface area and rich pore structure. FTIR results showed significant enhancement of peaks of oxygen-containing functional groups such as Fe-O, C=O, and O-H under co-pyrolysis of $\text{Fe}(\text{NO}_3)_3 \cdot 9\text{H}_2\text{O}$ and sawdust biochar. Kinetic fitting results showed that the adsorption mechanism was in line with the pseudo-second-order kinetic model, indicating that the adsorption process was mainly controlled by chemical interactions. The adsorption isotherm fitting results showed that both the Langmuir and

Freundlich isotherm models can fit the Fe₃O₄@BC adsorption process, indicating that monolayer and multilayer adsorption occur simultaneously.

In the Fe₃O₄@BC/PS system, the removal rate of AO7 can reach 90% after 20 min of reaction when the dosage of PS is 15 mM and the dosage of Fe₃O₄@BC is 2 g/L. •OH free radicals in the system perform a major role in degradation. Anions in water have an inhibitory effect on the degradation of AO7, with HCO₃⁻ > CO₃²⁻ > NO₃⁻ > Cl⁻ in descending order of inhibitory effect. Through DFT calculation of AO7 molecules, the analysis shows that -N=N- and sulfonic acid groups in AO7 molecules are the main reaction sites where chemical reactions are easy to occur.

This study shows that Fe₃O₄@BC biochar material has great potential in activating PS advanced oxidation to degrade water pollutants and has unique advantages in the treatment of refractory organic pollutants, such as AO7 in water.

Author Contributions: Conceptualization, Q.Z. and K.Z.; methodology, Q.Z.; investigation, J.X., X.W. and L.S.; resources, C.L.; data curation, Q.Z. and C.L.; writing—original draft preparation, Q.Z.; J.X., X.W., L.S. and S.; writing—review and editing, S., C.L. and E.L.; supervision, C.L. and E.L.; project administration, C.L.; funding acquisition, C.L. All authors have read and agreed to the published version of the manuscript.

Funding: This work was supported by the Natural Science Foundation of Shanghai (No. 20ZR1438200) and the National Natural Science Foundation of China (No. 51778565).

Data Availability Statement: Not applicable.

Conflicts of Interest: The authors declare no conflict of interest.

References

1. Mahdi Ahmed, M.; Barbati, S.; Doumenq, P.; Chiron, S. Sulfate radical anion oxidation of diclofenac and sulfamethoxazole for water decontamination. *Chem. Eng. J.* **2012**, *197*, 440–447. [[CrossRef](#)]
2. Ghauch, A.; Tuqan, A.M. Oxidation of bisoprolol in heated persulfate/H₂O systems: Kinetics and products. *Chem. Eng. J.* **2012**, *183*, 162–171. [[CrossRef](#)]
3. Qian, L.; Kopinke, F.-D.; Scherzer, T.; Griebel, J.; Georgi, A. Enhanced degradation of perfluorooctanoic acid by heat-activated persulfate in the presence of zeolites. *Chem. Eng. J.* **2022**, *429*, 132500. [[CrossRef](#)]
4. Ding, X.; Song, X.; Chen, X.; Ding, D.; Xu, C.; Chen, H. Degradation and mechanism of hexafluoropropylene oxide dimer acid by thermally activated persulfate in aqueous solutions. *Chemosphere* **2022**, *286*, 131720. [[CrossRef](#)]
5. Shah, N.S.; Khan, J.A.; Sayed, M.; Khan, Z.U.H.; Rizwan, A.D.; Muhammad, N.; Boczkaj, G.; Murtaza, B.; Imran, M.; Khan, H.M.; et al. Solar light driven degradation of norfloxacin using as-synthesized Bi³⁺ and Fe²⁺ co-doped ZnO with the addition of HSO₅⁻: Toxicities and degradation pathways investigation. *Chem. Eng. J.* **2018**, *351*, 841–855. [[CrossRef](#)]
6. Kordestani, B.; Jalilzadeh Yengejeh, R.; Takdastan, A.; Neisi, A.K. A new study on photocatalytic degradation of meropenem and ceftriaxone antibiotics based on sulfate radicals: Influential factors, biodegradability, mineralization approach. *Microchem. J.* **2019**, *146*, 286–292. [[CrossRef](#)]
7. Ni, T.; Yang, Z.; Zhang, H.; Zhou, L.; Guo, W.; Pan, L.; Yang, Z.; Chang, K.; Ge, C.; Liu, D. Peroxymonosulfate activation by Co₃O₄/SnO₂ for efficient degradation of ofloxacin under visible light. *J. Colloid Interface Sci.* **2022**, *615*, 650–662. [[CrossRef](#)]
8. Matthaiou, V.; Frontistis, Z.; Petala, A.; Solakidou, M.; Deligiannakis, Y.; Angelopoulos, G.N.; Mantzavinos, D. Utilization of raw red mud as a source of iron activating the persulfate oxidation of paraben. *Process Saf. Environ. Prot.* **2018**, *119*, 311–319. [[CrossRef](#)]
9. Ma, Q.; Zhang, X.; Guo, R.; Zhang, H.; Cheng, Q.; Xie, M.; Cheng, X. Persulfate activation by magnetic γ-Fe₂O₃/Mn₃O₄ nanocomposites for degradation of organic pollutants. *Sep. Purif. Technol.* **2019**, *210*, 335–342. [[CrossRef](#)]
10. Zhao, Y.S.; Sun, C.; Sun, J.Q.; Zhou, R. Kinetic modeling and efficiency of sulfate radical-based oxidation to remove p-nitroaniline from wastewater by persulfate/Fe₃O₄ nanoparticles process. *Sep. Purif. Technol.* **2015**, *142*, 182–188. [[CrossRef](#)]
11. Zhao, Q.; Mao, Q.; Zhou, Y.; Wei, J.; Liu, X.; Yang, J.; Luo, L.; Zhang, J.; Chen, H.; Chen, H.; et al. Metal-free carbon materials-catalyzed sulfate radical-based advanced oxidation processes: A review on heterogeneous catalysts and applications. *Chemosphere* **2017**, *189*, 224–238. [[CrossRef](#)] [[PubMed](#)]
12. Duan, X.; Sun, H.; Kang, J.; Wang, Y.; Indrawirawan, S.; Wang, S. Insights into Heterogeneous Catalysis of Persulfate Activation on Dimensional-Structured Nanocarbons. *ACS Catal.* **2015**, *5*, 4629–4636. [[CrossRef](#)]
13. Tang, L.; Liu, Y.; Wang, J.; Zeng, G.; Deng, Y.; Dong, H.; Feng, H.; Wang, J.; Peng, B. Enhanced activation process of persulfate by mesoporous carbon for degradation of aqueous organic pollutants: Electron transfer mechanism. *Appl. Catal. B Environ.* **2018**, *231*, 1–10. [[CrossRef](#)]

14. Liu, D.; Li, C.; Zhao, C.; Zhao, Q.; Niu, T.; Pan, L.; Xu, P.; Zhang, F.; Wu, W.; Ni, T. Facile synthesis of three-dimensional hollow porous carbon doped polymeric carbon nitride with highly efficient photocatalytic performance. *Chem. Eng. J.* **2022**, *438*, 135623. [[CrossRef](#)]
15. Duan, X.; Sun, H.; Ao, Z.; Zhou, L.; Wang, G.; Wang, S. Unveiling the active sites of graphene-catalyzed peroxymonosulfate activation. *Carbon* **2016**, *107*, 371–378. [[CrossRef](#)]
16. Liu, D.; Li, H.; Gao, R.; Zhao, Q.; Yang, Z.; Gao, X.; Wang, Z.; Zhang, F.; Wu, W. Enhanced visible light photoelectrocatalytic degradation of tetracycline hydrochloride by I and P co-doped TiO₂ photoelectrode. *J. Hazard. Mater.* **2021**, *406*, 124309. [[CrossRef](#)]
17. Wang, C.; Sun, R.; Huang, R.; Wang, H. Superior fenton-like degradation of tetracycline by iron loaded graphitic carbon derived from microplastics: Synthesis, catalytic performance, and mechanism. *Sep. Purif. Technol.* **2021**, *270*, 118773. [[CrossRef](#)]
18. Chokejaroenrat, C.; Sakulthaew, C.; Angkaew, A.; Satapanajaru, T.; Poapolathep, A.; Chirasatienpon, T. Remediating sulfadimethoxine-contaminated aquaculture wastewater using ZVI-activated persulfate in a flow-through system. *Aquac. Eng.* **2019**, *84*, 99–105. [[CrossRef](#)]
19. Hu, L.; Wang, P.; Liu, G.; Zheng, Q.; Zhang, G. Catalytic degradation of p-nitrophenol by magnetically recoverable Fe₃O₄ as a persulfate activator under microwave irradiation. *Chemosphere* **2020**, *240*, 124977. [[CrossRef](#)]
20. Li, Y.; Xiang, W.; Zhou, T.; Huang, M.; Wang, C.; Wu, X.; Mao, J.; Wang, P. Visible light induced efficient activation of persulfate by a carbon quantum dots (CQDs) modified γ -Fe₂O₃ catalyst. *Chin. Chem. Lett.* **2020**, *31*, 2757–2761. [[CrossRef](#)]
21. Yin, R.; Sun, J.; Xiang, Y.; Shang, C. Recycling and reuse of rusted iron particles containing core-shell Fe-FeOOH for ibuprofen removal: Adsorption and persulfate-based advanced oxidation. *J. Clean. Prod.* **2018**, *178*, 441–448. [[CrossRef](#)]
22. Fu, D.; Kurniawan, T.A.; Lin, L.; Li, Y.; Avtar, R.; Dzarfan Othman, M.H.; Li, F. Arsenic removal in aqueous solutions using FeS₂. *J. Env. Manag.* **2021**, *286*, 112246. [[CrossRef](#)] [[PubMed](#)]
23. Yan, J.; Han, L.; Gao, W.; Xue, S.; Chen, M. Biochar supported nanoscale zerovalent iron composite used as persulfate activator for removing trichloroethylene. *Bioresour. Technol.* **2015**, *175*, 269–274. [[CrossRef](#)]
24. Huong, P.T.; Jitae, K.; Al Tahtamouni, T.M.; Le Minh Tri, N.; Kim, H.-H.; Cho, K.H.; Lee, C. Novel activation of peroxymonosulfate by biochar derived from rice husk toward oxidation of organic contaminants in wastewater. *J. Water Process Eng.* **2020**, *33*, 101037. [[CrossRef](#)]
25. Kemmou, L.; Frontistis, Z.; Vakros, J.; Manariotis, I.D.; Mantzavinos, D. Degradation of antibiotic sulfamethoxazole by biochar-activated persulfate: Factors affecting the activation and degradation processes. *Catal. Today* **2018**, *313*, 128–133. [[CrossRef](#)]
26. Ouyang, D.; Yan, J.; Qian, L.; Chen, Y.; Han, L.; Su, A.; Zhang, W.; Ni, H.; Chen, M. Degradation of 1,4-dioxane by biochar supported nano magnetite particles activating persulfate. *Chemosphere* **2017**, *184*, 609–617. [[CrossRef](#)]
27. Xu, L.; Gao, H.; Shi, Y.; Zhao, Y. The heterogeneous volume-volatility relations in the exchange-traded fund market: Evidence from China. *Econ. Model.* **2020**, *85*, 400–408. [[CrossRef](#)]
28. Ouyang, D.; Chen, Y.; Yan, J.; Qian, L.; Han, L.; Chen, M. Activation mechanism of peroxymonosulfate by biochar for catalytic degradation of 1,4-dioxane: Important role of biochar defect structures. *Chem. Eng. J.* **2019**, *370*, 614–624. [[CrossRef](#)]
29. Kohantorabi, M.; Moussavi, G.; Giannakis, S. A review of the innovations in metal- and carbon-based catalysts explored for heterogeneous peroxymonosulfate (PMS) activation, with focus on radical vs. non-radical degradation pathways of organic contaminants. *Chem. Eng. J.* **2021**, *411*, 127957. [[CrossRef](#)]
30. Yu, J.; Wang, Y.; Han, D.; Cao, W.; Zheng, L.; Xie, Z.; Liu, H. Identification of Streptococcus mutans genes involved in fluoride resistance by screening of a transposon mutant library. *Mol. Oral Microbiol.* **2020**, *35*, 260–270. [[CrossRef](#)]
31. Zhang, X.; Zhang, P.; Yuan, X.; Li, Y.; Han, L. Effect of pyrolysis temperature and correlation analysis on the yield and physicochemical properties of crop residue biochar. *Bioresour. Technol.* **2020**, *296*, 122318. [[CrossRef](#)] [[PubMed](#)]
32. Bai, X.; Li, J.; Jia, C.; Shao, J.; Yang, Q.; Chen, Y.; Yang, H.; Wang, X.; Chen, H. Preparation of furfural by catalytic pyrolysis of cellulose based on nano Na/Fe-solid acid. *Fuel* **2019**, *258*, 116089. [[CrossRef](#)]
33. Zhuang, Y.; Yuan, S.; Liu, J.; Zhang, Y.; Du, H.; Wu, C.; Zhao, P.; Chen, H.; Pei, Y. Synergistic effect and mechanism of mass transfer and catalytic oxidation of octane degradation in yolk-shell Fe₃O₄@C/Fenton system. *Chem. Eng. J.* **2020**, *379*, 122262. [[CrossRef](#)]
34. Sun, H.W.; Chen, T.; Kong, L.J.; Cai, Q.; Xiong, Y.; Tian, S.H. Potential of Sludge Carbon as New Granular Electrodes for Degradation of Acid Orange 7. *Ind. Eng. Chem. Res.* **2015**, *54*, 5468–5474. [[CrossRef](#)]
35. Biswas, P.; Ainabayev, A.; Zhussupbekova, A.; Jose, F.; O'Connor, R.; Kaisha, A.; Walls, B.; Shvets, I.V. Tuning of oxygen vacancy-induced electrical conductivity in Ti-doped hematite films and its impact on photoelectrochemical water splitting. *Sci. Rep.* **2020**, *10*, 7463. [[CrossRef](#)]
36. Lee, Y.-C.; Li, Y.-F.; Chen, M.-J.; Chen, Y.-C.; Kuo, J.; Lo, S.-L. Efficient decomposition of perfluorooctanic acid by persulfate with iron-modified activated carbon. *Water Res.* **2020**, *174*, 115618. [[CrossRef](#)]
37. Yew, Y.P.; Shameli, K.; Miyake, M.; Kuwano, N.; Bt Ahmad Khairudin, N.B.; Bt Mohamad, S.E.; Lee, K.X. Green Synthesis of Magnetite (Fe₃O₄) Nanoparticles Using Seaweed (*Kappaphycus alvarezii*) Extract. *Nanoscale Res. Lett.* **2016**, *11*, 276. [[CrossRef](#)]
38. Radoń, A.; Drygała, A.; Hawełek, Ł.; Łukowiec, D. Structure and optical properties of Fe₃O₄ nanoparticles synthesized by co-precipitation method with different organic modifiers. *Mater. Charact.* **2017**, *131*, 148–156. [[CrossRef](#)]

39. Feng, Z.; Yuan, R.; Wang, F.; Chen, Z.; Zhou, B.; Chen, H. Preparation of magnetic biochar and its application in catalytic degradation of organic pollutants: A review. *Sci. Total Environ.* **2021**, *765*, 142673. [[CrossRef](#)]
40. Cui, X.; Zhang, S.-S.; Geng, Y.; Zhen, J.; Zhan, J.; Cao, C.; Ni, S.-Q. Synergistic catalysis by Fe₃O₄-biochar/peroxymonosulfate system for the removal of bisphenol a. *Sep. Purif. Technol.* **2021**, *276*, 119351. [[CrossRef](#)]
41. Wang, Y.; Sun, H.; Duan, X.; Ang, H.M.; Tadé, M.O.; Wang, S. A new magnetic nano zero-valent iron encapsulated in carbon spheres for oxidative degradation of phenol. *Appl. Catal. B Environ.* **2015**, *172–173*, 73–81. [[CrossRef](#)]
42. Bourahla, S.; Nemchi, F.; Belayachi, H.; Belayachi, A.; Harrats, C.; Belhakem, M. Removal of the AO7 dye by adsorption on activated carbon based on grape marc: Equilibrium, regeneration, and FTIR spectroscopy. *J. Iran. Chem. Soc.* **2023**, *20*, 669–681. [[CrossRef](#)]
43. Scheufele, F.B.; Módenes, A.N.; Borba, C.E.; Ribeiro, C.; Espinoza-Quiñones, F.R.; Bergamasco, R.; Pereira, N.C. Monolayer–multilayer adsorption phenomenological model: Kinetics, equilibrium and thermodynamics. *Chem. Eng. J.* **2016**, *284*, 1328–1341. [[CrossRef](#)]
44. Li, J.; Du, Y.; Deng, B.; Zhu, K.; Zhang, H. Activated carbon adsorptive removal of azo dye and peroxydisulfate regeneration: From a batch study to continuous column operation. *Environ. Sci. Pollut. Res.* **2017**, *24*, 4932–4941. [[CrossRef](#)] [[PubMed](#)]
45. Tan, C.; Jian, X.; Dong, Y.; Lu, X.; Liu, X.; Xiang, H.; Cui, X.; Deng, J.; Gao, H. Activation of peroxymonosulfate by a novel EGCE@Fe₃O₄ nanocomposite: Free radical reactions and implication for the degradation of sulfadiazine. *Chem. Eng. J.* **2019**, *359*, 594–603. [[CrossRef](#)]
46. Muhammad, S.; Shukla, P.R.; Tadé, M.O.; Wang, S. Heterogeneous activation of peroxymonosulphate by supported ruthenium catalysts for phenol degradation in water. *J. Hazard. Mater.* **2012**, *215–216*, 183–190. [[CrossRef](#)]
47. Tan, C.; Gao, N.; Deng, Y.; Deng, J.; Zhou, S.; Li, J.; Xin, X. Radical induced degradation of acetaminophen with Fe₃O₄ magnetic nanoparticles as heterogeneous activator of peroxymonosulfate. *J. Hazard. Mater.* **2014**, *276*, 452–460. [[CrossRef](#)] [[PubMed](#)]
48. Zhu, Y.; Yue, M.; Natarajan, V.; Kong, L.; Ma, L.; Zhang, Y.; Zhao, Q.; Zhan, J. Efficient activation of persulfate by Fe₃O₄@β-cyclodextrin nanocomposite for removal of bisphenol A. *RSC Adv.* **2018**, *8*, 14879–14887. [[CrossRef](#)]
49. Tang, J.; Ma, Y.; Zeng, C.; Yang, L.; Cui, S.; Zhi, S.; Yang, F.; Ding, Y.; Zhang, K.; Zhang, Z. Fe-Al bimetallic oxides functionalized-biochar via ball milling for enhanced adsorption of tetracycline in water. *Bioresour. Technol.* **2023**, *369*, 128385. [[CrossRef](#)]
50. Zhang, X.; Zhang, J.; Huang, X.; Wu, Q.P.; Yan, C.H.; Lu, J.F. Efficient peroxymonosulfate activation by Zn/Fe metal-organic framework-derived ZnO/Fe₃O₄@carbon spheres for the degradation of Acid Orange 7. *Water Environ. Res.* **2019**, *91*, 634–641. [[CrossRef](#)]
51. Wang, J.; Wang, S. Effect of inorganic anions on the performance of advanced oxidation processes for degradation of organic contaminants. *Chem. Eng. J.* **2021**, *411*, 128392. [[CrossRef](#)]
52. Chen, S.; Cai, M.; Liu, Y.; Zhang, L.; Feng, L. Effects of water matrices on the degradation of naproxen by reactive radicals in the UV/peracetic acid process. *Water Res.* **2019**, *150*, 153–161. [[CrossRef](#)] [[PubMed](#)]
53. Zhou, L.; Zheng, W.; Ji, Y.; Zhang, J.; Zeng, C.; Zhang, Y.; Wang, Q.; Yang, X. Ferrous-activated persulfate oxidation of arsenic(III) and diuron in aquatic system. *J. Hazard. Mater.* **2013**, *263*, 422–430. [[CrossRef](#)] [[PubMed](#)]
54. Liu, S.; Zhang, Z.; Huang, F.; Liu, Y.; Feng, L.; Jiang, J.; Zhang, L.; Qi, F.; Liu, C. Carbonized polyaniline activated peroxymonosulfate (PMS) for phenol degradation: Role of PMS adsorption and singlet oxygen generation. *Appl. Catal. B Environ.* **2021**, *286*, 119921. [[CrossRef](#)]
55. Wang, H.; Guo, W.; Si, Q.; Liu, B.; Zhao, Q.; Luo, H.; Ren, N. Non-covalent doping of carbon nitride with biochar: Boosted peroxymonosulfate activation performance and unexpected singlet oxygen evolution mechanism. *Chem. Eng. J.* **2021**, *418*, 129504. [[CrossRef](#)]
56. Long, Y.; Li, S.; Yang, P.; Chen, X.; Liu, W.; Zhan, X.; Xue, C.; Liu, D.; Huang, W. Synthesis of ZIF-67 derived honeycomb porous Co/NC catalyst for AO7 degradation via activation of peroxymonosulfate. *Sep. Purif. Technol.* **2022**, *286*, 120470. [[CrossRef](#)]
57. Xu, Y.; Ai, J.; Zhang, H. The mechanism of degradation of bisphenol A using the magnetically separable CuFe₂O₄/peroxymonosulfate heterogeneous oxidation process. *J. Hazard. Mater.* **2016**, *309*, 87–96. [[CrossRef](#)]
58. Wang, C.; Shi, P.; Cai, X.; Xu, Q.; Zhou, X.; Zhou, X.; Yang, D.; Fan, J.; Min, Y.; Ge, H.; et al. Synergistic Effect of Co₃O₄ Nanoparticles and Graphene as Catalysts for Peroxymonosulfate-Based Orange II Degradation with High Oxidant Utilization Efficiency. *J. Phys. Chem. C* **2016**, *120*, 336–344. [[CrossRef](#)]
59. Zhong, H.; Brusseau, M.L.; Wang, Y.; Yan, N.; Quig, L.; Johnson, G.R. In-situ activation of persulfate by iron filings and degradation of 1,4-dioxane. *Water Res.* **2015**, *83*, 104–111. [[CrossRef](#)]
60. Temiz, K.; Olmez-Hanci, T.; Arslan-Alaton, I. Zero-valent iron-activated persulfate oxidation of a commercial alkyl phenol polyethoxylate. *Environ. Technol.* **2016**, *37*, 1757–1767. [[CrossRef](#)]
61. Yi, X.-H.; Ji, H.; Wang, C.-C.; Li, Y.; Li, Y.-H.; Zhao, C.; Wang, A.; Fu, H.; Wang, P.; Zhao, X.; et al. Photocatalysis-activated SR-AOP over PDINH/MIL-88A(Fe) composites for boosted chloroquine phosphate degradation: Performance, mechanism, pathway and DFT calculations. *Appl. Catal. B Environ.* **2021**, *293*, 120229. [[CrossRef](#)]
62. Zhao, C.; Wang, J.; Chen, X.; Wang, Z.; Ji, H.; Chen, L.; Liu, W.; Wang, C.-C. Bifunctional Bi₁₂O₁₇Cl₂/MIL-100(Fe) composites toward photocatalytic Cr(VI) sequestration and activation of persulfate for bisphenol A degradation. *Sci. Total Environ.* **2021**, *752*, 141901. [[CrossRef](#)] [[PubMed](#)]

63. Zhang, J.; Shao, X.; Shi, C.; Yang, S. Decolorization of Acid Orange 7 with peroxymonosulfate oxidation catalyzed by granular activated carbon. *Chem. Eng. J.* **2013**, *232*, 259–265. [[CrossRef](#)]
64. Li, F.; Duan, F.; Ji, W.; Gui, X. Biochar-activated persulfate for organic contaminants removal: Efficiency, mechanisms and influencing factors. *Ecotoxicol. Environ. Saf.* **2020**, *198*, 110653. [[CrossRef](#)] [[PubMed](#)]

Disclaimer/Publisher’s Note: The statements, opinions and data contained in all publications are solely those of the individual author(s) and contributor(s) and not of MDPI and/or the editor(s). MDPI and/or the editor(s) disclaim responsibility for any injury to people or property resulting from any ideas, methods, instructions or products referred to in the content.